nature physics

Supplementary information

https://doi.org/10.1038/s41567-026-03405-1

Altermagnetic photonic crystals

In the format provided by the
authors and unedited

Contents

Supplementary Note 1. First-principles Maxwell derivation.

We start from the TM-polarized Maxwell equation in gyromagnetic media, where the permeability tensor contains an off-diagonal component $\mu_k(\mathbf{r})$. Eliminating the in-plane magnetic fields gives a scalar equation for E_z, $\nabla\cdot[\alpha(\mathbf{r})\nabla E_z]-\boldsymbol{\Gamma}(\mathbf{r})\cdot\nabla E_z+\omega^2\varepsilon_0\mu_0\varepsilon(\mathbf{r})E_z=0$, with the material-dependent coefficients $\alpha(\mathbf{r})=\frac{\mu_r(\mathbf{r})}{\mu_r^2(\mathbf{r})-\mu_k^2(\mathbf{r})}$, $\boldsymbol{\Gamma}(\mathbf{r})=\left[\frac{\partial\beta(\mathbf{r})}{\partial y},-\frac{\partial\beta(\mathbf{r})}{\partial x}\right]$, $\beta(\mathbf{r})=-\frac{i\mu_k(\mathbf{r})}{\mu_r^2(\mathbf{r})-\mu_k^2(\mathbf{r})}$. The key quantity is thus the spatial variation of the gyrotropic field $\beta(\mathbf{r})$, controlled by the lattice geometry and magnetization pattern.

Consider a square Bravais lattice containing two sublattices A and B at internal positions $\boldsymbol{\tau}_A$ and $\boldsymbol{\tau}_B$. The gyrotropic field is modelled as a superposition of localized profiles, $\beta(\mathbf{r})=\beta_0\sum_{\mathbf{R}}[s_A f(\mathbf{r}-\mathbf{R}-\boldsymbol{\tau}_A)+s_B f(\mathbf{r}-\mathbf{R}-\boldsymbol{\tau}_B)]$, where the signs $s_{A,B}=\pm1$ encode the magnetization direction. Because $\beta(\mathbf{r})$ is periodic, its Fourier components factorize into $\beta_{\mathbf{G}}=\beta_0 F(\mathbf{G})S(\mathbf{G})$. Here, $F(\mathbf{G})$ is the form factor of one scatterer (decays rapidly with $|\mathbf{G}|$). $S(\mathbf{G})$ is the structure factor determined solely by $\boldsymbol{\tau}_{A,B}$ and $s_{A,B}$.

For uniform magnetization ($s_A=s_B$), $S(\mathbf{G})$ peaks at $\mathbf{G}=0$. Hence $\beta(\mathbf{r})$ is nearly constant, implying $\boldsymbol{\Gamma}(\mathbf{r})\simeq 0$. The scalar equation reduces to $\nabla\cdot[\alpha(\mathbf{r})\nabla E_z]+\omega^2\varepsilon_0\mu_0\varepsilon(\mathbf{r})E_z=0$. This yields only a momentum-independent (Zeeman-type) polarization splitting with no **k**-dependent dispersion. In contrast, for opposite magnetization $s_A=-s_B$, $S(\mathbf{G})\propto\sin(\mathbf{G}\cdot\boldsymbol{\delta}/2)$ with $\boldsymbol{\delta}=\boldsymbol{\tau}_B-\boldsymbol{\tau}_A$. The $\mathbf{G}=0$ terms cancels, shifting the dominant weight to finite-**G**. Thus $\beta(\mathbf{r})$ becomes oscillatory, and $\boldsymbol{\Gamma}(\mathbf{r})$ acquires nonzero Bloch harmonics, enabling momentum-dependent gyrotropic coupling.

Applying Bloch's theorem $E_z(\mathbf{r})=u_k(\mathbf{r})e^{i\mathbf{k}\cdot\mathbf{r}}$ gives an equation for the periodic part u_k. The chiral term contributes schematically as $\boldsymbol{\Gamma}\cdot[(\nabla+i\mathbf{k})u_k]$, and after expanding $u_k(\mathbf{r})$ and $\boldsymbol{\Gamma}(\mathbf{r})$ into reciprocal-lattice components, one finds that $\boldsymbol{\Gamma}_{\mathbf{G}}$ scatters the state at $\mathbf{k}$ to $\mathbf{k}+\mathbf{G}$. Keeping only the dominant Fourier channel (main-band approximation), the chiral coupling reduces to an effective odd-in-$\mathbf{k}$ perturbation $V_{\mathrm{eff}}(\mathbf{k}) \sim \sum_{\mathbf{G}}(\mathbf{k} \cdot \boldsymbol{\Gamma}_{\mathbf{G}})$, which controls the polarization-dependent dispersion.

To obtain a compact low-energy Hamiltonian, we project the operator onto localized modes $w_A(\mathbf{r})$, $w_B(\mathbf{r})$ centered on the two sublattice, $u_k(\mathbf{r}) = c_A(\mathbf{k})w_A(\mathbf{r}) + c_B(\mathbf{k})w_B(\mathbf{r})$. This converts the Maxwell operator into a 2×2 Hermitian matrix $H_{\mathrm{eff}}(\mathbf{k}) = \Omega_0(\mathbf{k})\tau_0 + d_x(\mathbf{k})\tau_x + d_y(\mathbf{k})\tau_y + d_z(\mathbf{k})\tau_z$. Here, d_x arises from the reciprocal coupling $\nabla \cdot [\alpha(\mathbf{r})\nabla]$, d_y from the nonreciprocal gyrotropic coupling $\boldsymbol{\Gamma}(\mathbf{r}) \cdot \nabla$, and d_z from the A/B-asymmetric corrections created by the staggered $\boldsymbol{\Gamma}(\mathbf{r})$. Only the third term can generate an altermagnetic-type momentum dispersion.

For a square lattice, the A-A and B-B "bond" contribute cosine-type terms $d_z(\mathbf{k}) = \sum_\delta t_\delta \cos(\mathbf{k} \cdot \delta)$. Staggered gyrotropy imposes opposite signs between x and y channels: $t_x = -t_{-y} = t_{AM}$, giving the leading *d*-wave (B_{1g}) pattern $d_z(\mathbf{k}) = 2t_{AM}(\cos k_x a - \cos k_y a)$. This constitutes the photonic altermagnetic gap, producing momentum-dependent RCP/LCP splitting under zero net magnetization. In practice, slight geometric imbalance inevitably adds a small isotropic correction (*s*-wave), $d_z(\mathbf{k}) = 2t_{AM}(\cos k_x a - \cos k_y a) + 2\delta t(\cos k_x a + \cos k_y a)$, where $|\delta t| \ll |t_{AM}|$. The first term dominates, preserving the characteristic altermagnetic behaviour.

In electrons, altermagnetic comes from exchange-induced spin-splitting, while in photonics, the analogue arises from spatial gradient of the gyromagnetic tensor, not from local magnetization strength. The staggered magnetization pattern enforces a sign-alternating $\boldsymbol{\Gamma}(\mathbf{r})$, which in turn produces the *d*-wave polarization splitting characteristic of altermagnets. Because $\nabla\beta(\mathbf{r})$ is geometry-controlled, not symmetry-enforced, a pure B_{1g} form is never exact; nevertheless, the leading behaviour is robust and experimentally accessible.

It is important to note that, although a formal correspondence can be established between the photonic system and an effective altermagnetic Hamiltonian, this does not imply equivalence at the level of symmetry representation, operator algebra, or spin-group structure. This is because photonic polarization does not constitute a fermionic spin degree of freedom and does not obey the same symmetry representations or operator algebra that define electronic altermagnets. Therefore, the present results should be understood as a structural analogy rather than a fundamental equivalence.

Supplementary Note 2. Tight binding vs. photonic crystal distinctions.

We show how the bulk band evolves as the alternating-magnetization strength t_{AM} increases in the tight-binding altermagnetic Hamiltonian. When $t_{\mathrm{AM}} = 0$, the system retains full lattice symmetry and the two bands are completely degenerate, showing no spin (polarization) contrast (Supplementary Figure 1a). As t_{AM} is gradually introduced, the degeneracy is lifted along the X-M-Y path, producing two oppositely polarized branches whose separation grows monotonically with t_{AM} (Supplementary Figures 1b-1f). Importantly, the bands remain degenerate at the M point for all t_{AM}, reflecting the compensated magnetic configuration that enforces zero net magnetization. The increasing band splitting and alternating polarization texture confirm the emergence of the characteristic altermagnetic behavior governed by the *d*-wave term.

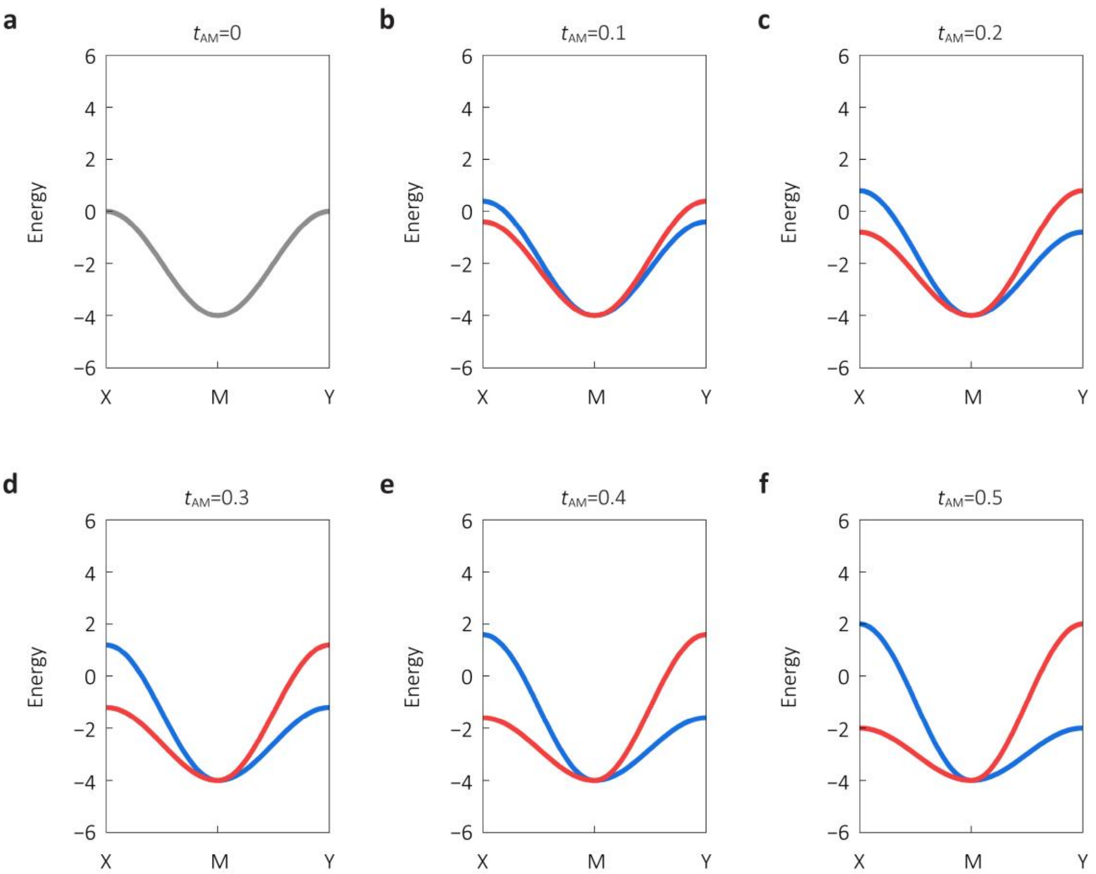

Supplementary Figure 1 | Bulk band with increasing alternating-magnetization strength t_{AM}. Simulated dispersions of the altermagnetic Hamiltonian for different t_{AM} values: **(a)** t_{AM}=0, **(b)** t_{AM}=0.1, **(c)** t_{AM}=0.2, **(d)** t_{AM}=0.3, **(e)** t_{AM}=0.4, and **(f)** t_{AM}=0.5.

When the magnetophotonic crystal preserves full mirror symmetry (d=d_1−d_2=0), the two bands remain degenerate in polarization, and the Stokes parameter is identically S_3=0 (Supplementary Figure 2a). This is because, unlike electrons whose intrinsic spin can couple to the exchange field even under high symmetry, photons possess only geometry-dependent polarization, and the σ_z channel is strictly forbidden by mirror symmetry. In contrast, when a small structural displacement is introduced (d=0.1a), mirror symmetry between the x and y directions is broken while the global $C_{4v}T$ symmetry is preserved. This controlled perturbation unlocks the σ_z channel, enabling momentum-dependent polarization splitting (Supplementary Figure 2b).

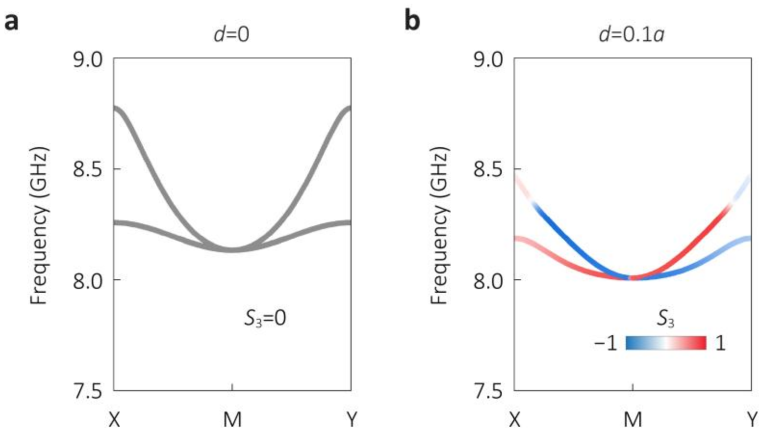

Supplementary Figure 2 | Mirror-symmetry breaking on the emergence of altermagnetic polarization splitting. (a) d=0. **(b)** d=0.1a.

It should be noted that the observed polarization splitting is not an artifact of gauge choice or longitudinal-field contamination. In both simulations and experiments, we solve the full vectorial Maxwell eigenproblem under the constraint $\nabla \cdot (\varepsilon \mathbf{E}) = 0$, ensuring that only transverse (divergence-free) components contribute to the eigenmodes and eliminating any spurious longitudinal admixture near degeneracy points. The polarization properties are extracted from the transverse magnetic-field components (H_x, H_y), using the gauge-independent Stokes parameter $S_3(\mathbf{k}) = -\frac{2\mathrm{Im}[H_x H_y^*]}{|H_x|^2+|H_y|^2}$. The momentum-dependent polarization splitting remains robust under strict enforcement of the divergence-free condition, confirming its genuine physical origin rather than numerical or gauge-related artifacts.

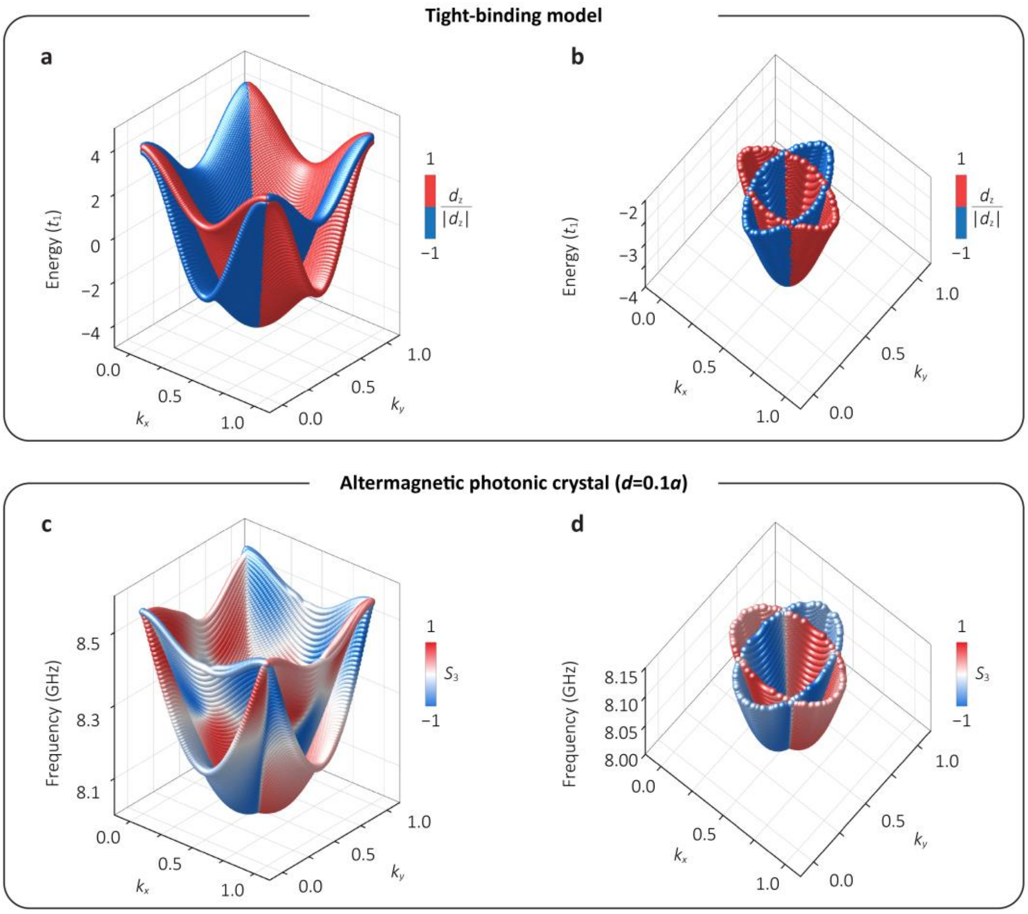

Supplementary Figure 3 | Electronic and photonic altermagnets. (a-b) Tight-binding model of a two-sublattice d-wave altermagnet. **(c-d)** Full-wave simulation of the altermagnetic photonic crystal with structural offset d=0.1a.

Unlike electronic altermagnets where spin is an intrinsic quantum degree of freedom, the photonic analogue is governed by polarization, which is inherently coupled to the field distribution and geometry of the photonic crystal. As a result, polarization purity cannot be perfectly maintained across the entire band: structural displacement, magnetic bias, and high-order multipole coupling all introduce weak mixing between right- and left-circular components, especially far from the near-degenerate region. This mixing manifests as the apparent high-frequency hybridization. However, this effect does not compromise the altermagnetic nature of the system. Near the degeneracy, where the d-wave term dominates, the bands exhibit clear momentum-dependent polarization splitting and opposite polarization textures, fully consistent with the defining characteristics of altermagnetic behavior. The high-frequency hybridization simply reflects the geometric sensitivity of photonic polarization, rather than a breakdown of the underlying symmetry mechanism. To make this distinction explicit, we have plotted both the tight-binding and photonic crystal band structures with spin- or polarization-resolved color maps. In electronic altermagnets, the spin texture is characterized by $s_z = \frac{d_z}{|d_z|}$, which remains well-defined throughout the Brillouin zone because the spin is an intrinsic quantum degree of freedom decoupled from lattice geometry (Supplementary Figures 3a-3b).

In contrast, in photonic crystals, the analogous quantity is given by the normalized Stokes parameter $S_3 = -2\mathrm{Im}(H_x H_y^*)/\left(|H_x|^2 + \left|H_y\right|^2\right)$, where H_x and H_y are the in-plane magnetic field components. Unlike electronic spin, which is an intrinsic quantum degree of freedom, S_3 depends on the local electromagnetic field distribution and thus is sensitive to geometric displacement, boundary conditions, and higher-order multipole coupling. As the frequency increases, these effects induce partial polarization mixing, leading to the observed hybridization at high frequencies. Nevertheless, near the degeneracy, the polarization remains well-defined and exhibits strong opposite-handed separation, confirming the robust altermagnetic behavior in the photonic regime (Supplementary Figures 3c-3d).

To enable a direct comparison between electrons and photons, we plot the full-Brillouin-zone distributions of the first two bands for both the tight-binding model and the photonic crystal, color-coded by spin and polarization respectively (Supplementary Figure 4). In the tight-binding model, spin is an intrinsic degree of freedom and therefore remains pure across the entire Brillouin zone, producing two sharply separated spin sectors (Supplementary Figures 4a-4b). In contrast, photonic polarization is not an intrinsic quantum number but emerges from geometry-dependent field configurations governed by Maxwell's equations. As a result, polarization cannot remain globally pure: away from the degeneracy point, local field mixing leads to regions where LCP and RCP components coexist. Crucially, around the M-point degeneracy, where altermagnetic splitting originates, the photonic crystal exhibits a large, continuous momentum region with highly pure and opposite polarizations (Supplementary Figures 4c-4d). In this regime, polarization behaves as an effective spin analogue and reproduces the momentum-selective splitting characteristic of fermionic altermagnets. This illustrates a key distinction and advantage of the photonic platform: although polarization purity is geometry-limited globally, it can be engineered to form wide momentum sectors of "spin-like" behavior around symmetry-protected degeneracies, which is sufficient to realize altermagnetic symmetry in photonic systems.

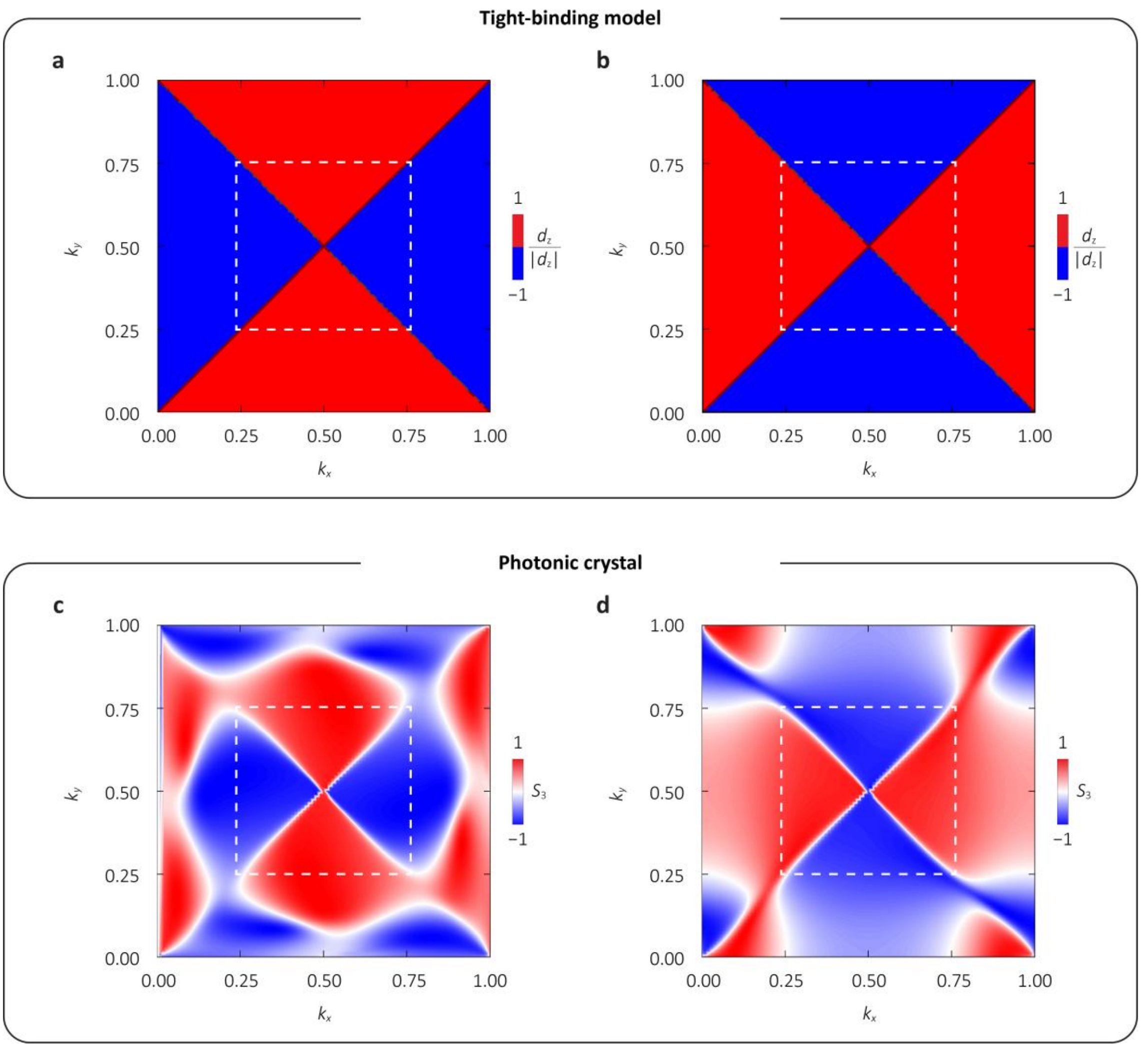

Supplementary Figure 4 | Comparison between tight-binding and photonic-crystal polarization textures. (**a-b**) Tight-binding model showing the spin texture of the first and second bands across the Brillouin zone. (**c-d**) Corresponding photonic-crystal results, with bands color-coded by the Stokes parameter S_3.

Supplementary Note 3. Derivation of the spin analogue.

Projecting the sublattice Hamiltonian onto the polarization subspace yields $H_{\text{pol}}(\mathbf{k}) = \bar{\Omega}_0(\mathbf{k})\sigma_0 + d_z(\mathbf{k})\sigma_z$, where σ_z acts on the polarization basis $|R\rangle = \frac{1}{\sqrt{2}}(\hat{x} - i\hat{y})$, $|L\rangle = \frac{1}{\sqrt{2}}(\hat{x} + i\hat{y})$, which play the role of "spin-up" and "spin-down" states for photons.

For a given Bloch mode at momentum $\mathbf{k}$, the transverse magnetic field can be written in the linear basis as the normalized Jones vector $|\psi\rangle = \frac{1}{\sqrt{|H_x|^2+|H_y|^2}}\begin{pmatrix} H_x(\mathbf{k}) \\ H_y(\mathbf{k}) \end{pmatrix}$. Expanding in the circular basis, $|\psi\rangle = c_R|R\rangle + c_L|L\rangle$, one finds the coefficients $c_R = \frac{H_x - iH_y}{\sqrt{2\left(|H_x|^2+|H_y|^2\right)}}$, $c_L = \frac{H_x + iH_y}{\sqrt{2\left(|H_x|^2+|H_y|^2\right)}}$. In the $|R\rangle$, $|L\rangle$ basis, $\sigma_z = \text{diag}(1, -1)$, so the expectation value of the pseudospin operator is $\langle\sigma_z\rangle = |c_R|^2 - |c_L|^2$. Substituting the expression of c_R and c_L and performing a straightforward algebraic simplification gives

$$\langle\sigma_z\rangle = -\frac{2\text{Im}\left[H_x(\mathbf{k})H_y^*(\mathbf{k})\right]}{|H_x(\mathbf{k})|^2+|H_y(\mathbf{k})|^2}.$$

In optics, the degree of circular polarization is quantified by the Stokes parameter

$$S_3(\mathbf{k}) = -\frac{2\text{Im}\left[H_x(\mathbf{k})H_y^*(\mathbf{k})\right]}{|H_x(\mathbf{k})|^2+|H_y(\mathbf{k})|^2}.$$

We therefore obtain the simple identification $\langle\sigma_z\rangle = S_3(\mathbf{k})$, i.e., the Stokes parameter S_3 is exactly the expectation value of the pseudospin operator σ_z. This established the one-to-one correspondence between optical polarization in our photonic crystal and the spin degree of freedom in fermionic altermagnets.

Supplementary Note 4. Spin analogue of a single gyromagnetic cylinder.

We provide additional simulations demonstrating that both the excitation scheme and the resulting polarization splitting are robust against variations in frequency and structural geometry. Supplementary Figure 5 presents the simulated electric-field amplitudes and Stokes parameter S_3 maps generated by four in-phase linear sources under opposite magnetic biases across 7.5~9.0 GHz. In all cases, the sources consistently produce well-defined circular polarization patterns, confirming that the chiral excitation remains stable over the entire operating bandwidth.

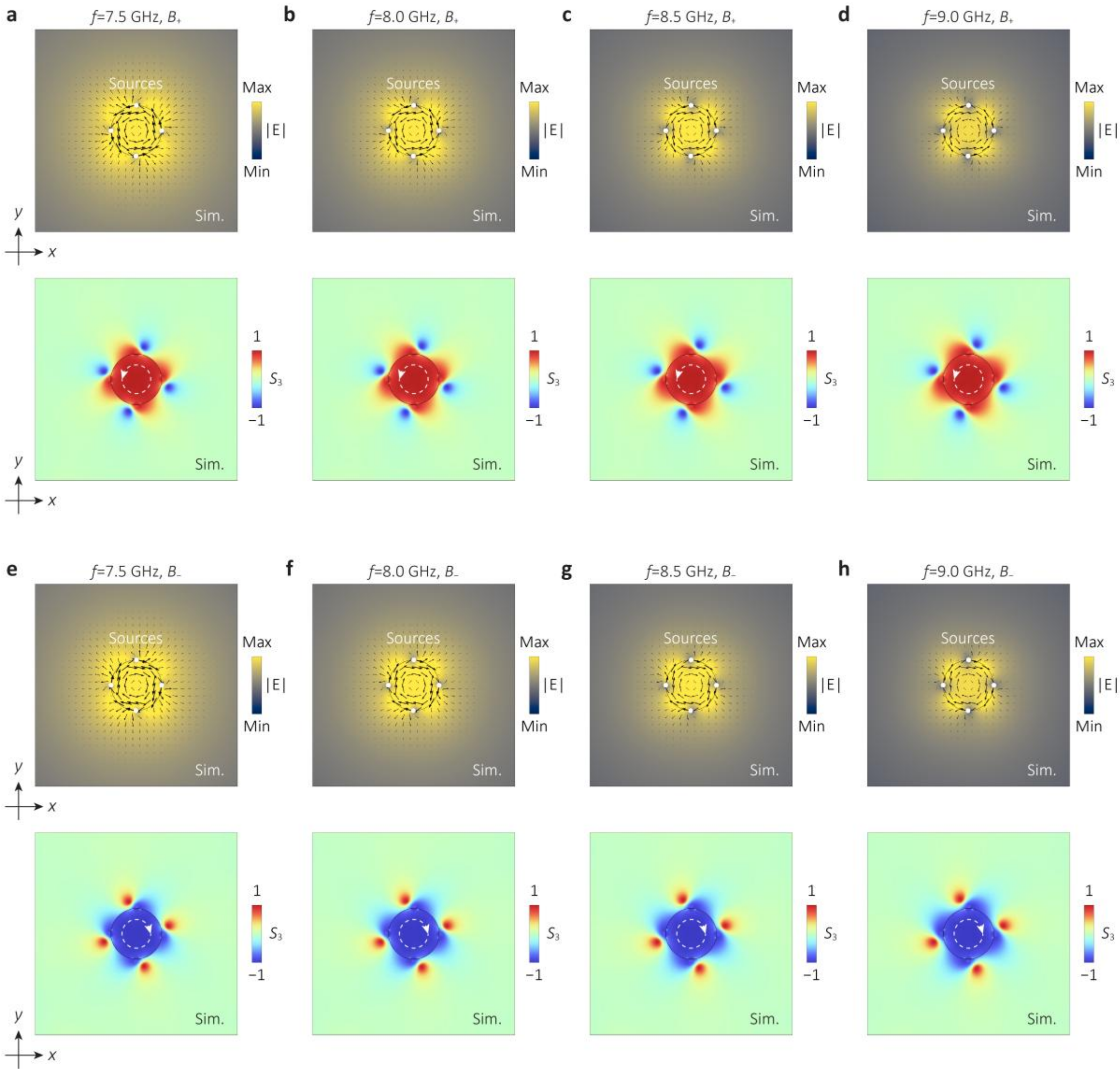

Supplementary Figure 5 | Simulated field distributions and polarization states of the excitation sources at different frequencies. (a-d) Simulated electric field amplitude |E| (top) and corresponding Stokes parameter S_3 maps (bottom) for four linear sources (white points) under magnetic bias B_+ at frequencies of 7.5, 8.0, 8.5, and 9.0 GHz, respectively. **(e-h)** Simulated electric field amplitude |E| (top) and corresponding Stokes parameter S_3 (bottom) for four linear sources (white points) under magnetic bias B_- at the same frequencies.

Supplementary Figure 6 further examines the role of structural geometry by comparing the field distributions and S_3 patterns for gyromagnetic elements shaped as quarter-circles, half-circles, and arbitrary distorted profiles. The results show that the observed polarization splitting is independent of the specific geometry of the gyromagnetic elements, confirming that the effect arises from time-reversal symmetry breaking rather than geometric resonances.

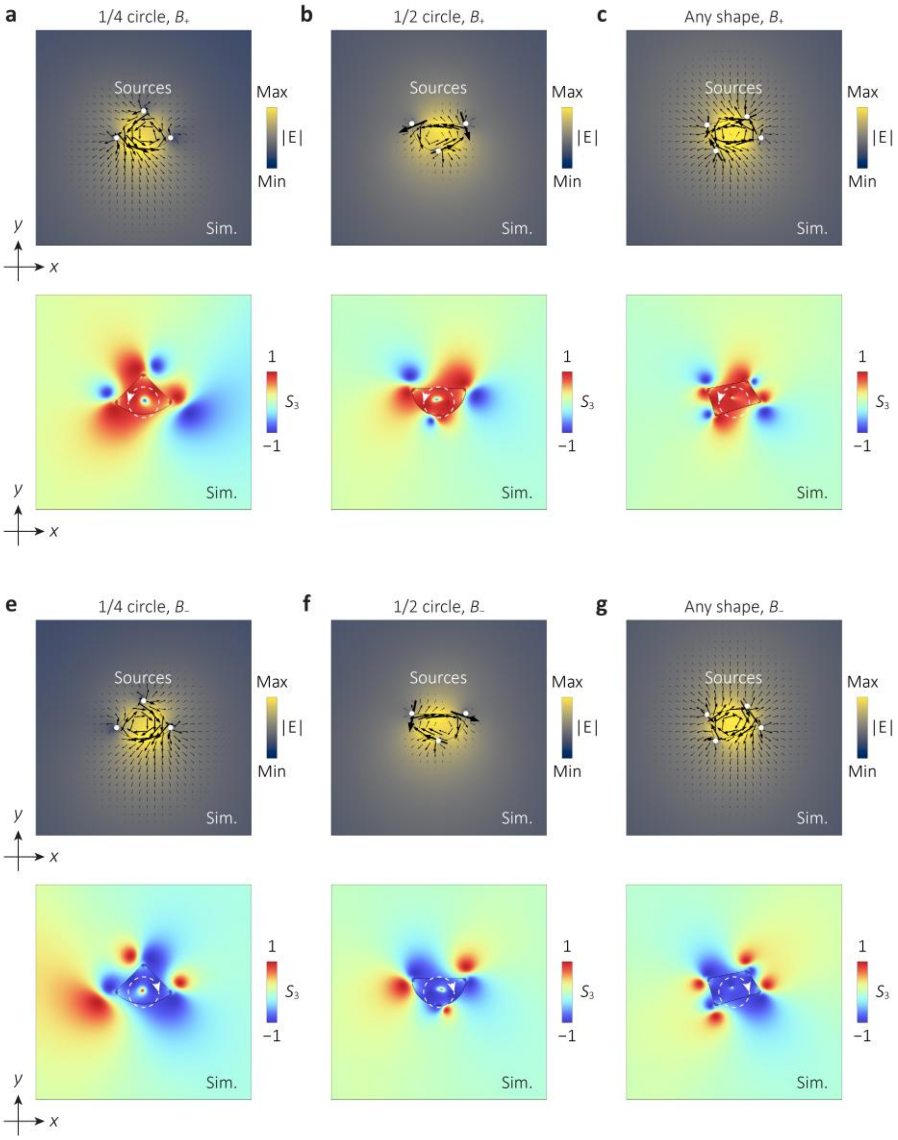

Supplementary Figure 6 | Robustness of polarization splitting against variations in structural shape. (a-c) Simulated electric field amplitude |E| (top) and Stokes parameter S_3

distributions (bottom) for linear sources under magnetic bias B+ with different pillar geometries: quarter-circle, half-circle, and arbitrary shapes. **(e-g)** Corresponding simulations for linear sources under magnetic bias B_{-}.

Supplementary Note 5. Bulk band of a displaced structure without magnetic bias.

We compute the photonic band structures for a series of structural offsets ranging from d from 0 to $0.14a$ while completely removing the gyromagnetic response ($\mu_k = 0$). Across all cases, the bands remain nearly degenerate with only negligible polarization contrast, even at the largest displacement (Supplementary Figure 7). This confirms that breaking the *x*-*y* geometric equivalence, though necessary for enabling altermagnetic coupling, cannot by itself produce momentum-dependent spin-like splitting. Time-reversal-symmetry breaking, introduced by the staggered magnetic bias, is indispensable for realizing the full altermagnetic dispersions.

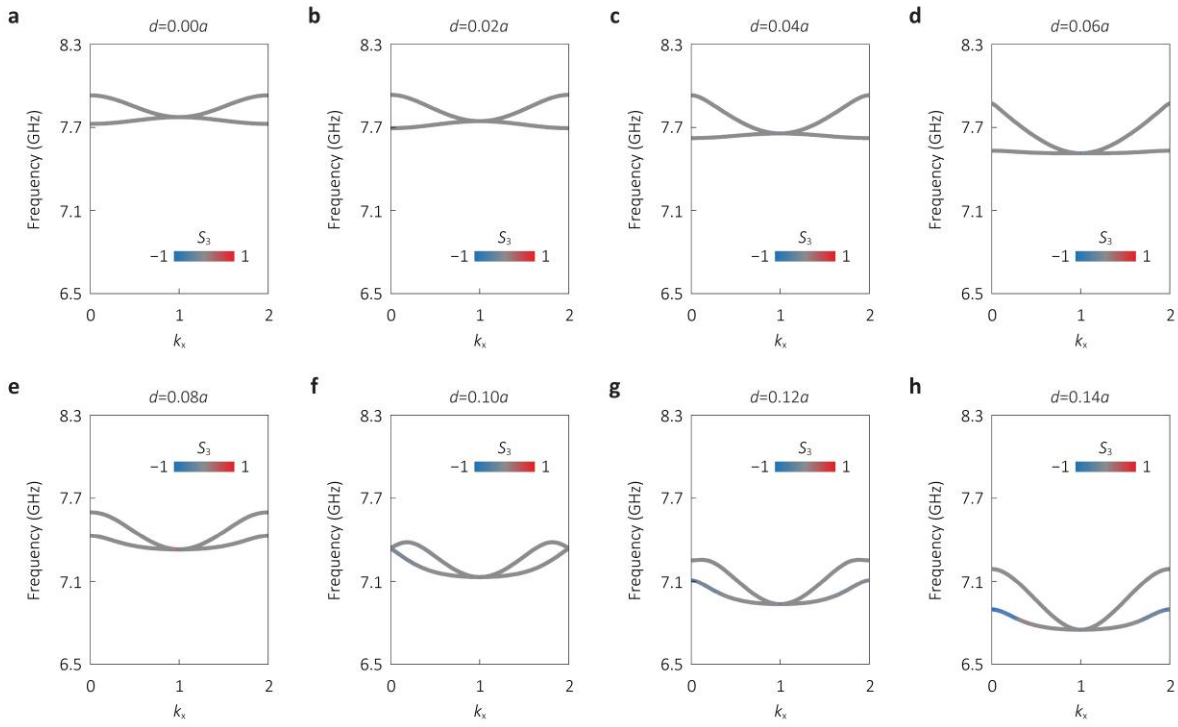

Supplementary Figure 7 | Photonic band structure as a function of structural displacement *d* in the absence of magnetization ($\mu_k = 0$). Simulated band diagrams for displacements ranging from d=0 to $0.14a$. Almost no polarization splitting is observed even when a finite displacement is introduced.

Supplementary Note 6. Programmable magnetic patterning for phase reconfiguration.

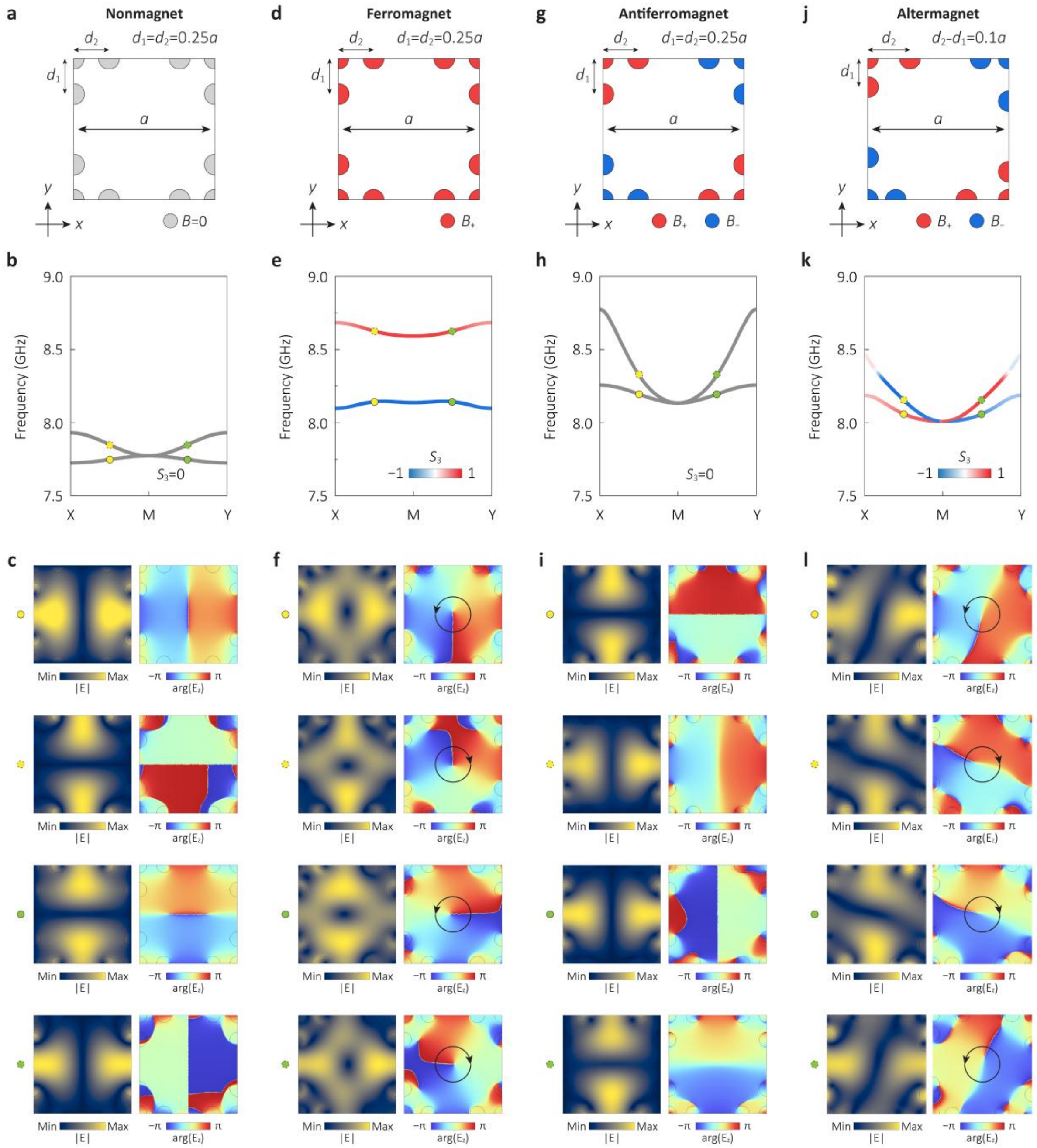

Supplementary Figure 8 | Evolution of photonic band structures and eigenmodes across nonmagnetic, ferromagnetic, antiferromagnetic, and altermagnetic phases. (a, d, g, j) Schematics of the four configurations: **(a)** nonmagnet, **(d)** ferromagnet, **(g)** antiferromagnet, and **(j)** altermagnet. Red and blue circles indicate gyromagnetic elements with opposite magnetic biases along the z direction, while gray circles represent unbiased elements. The displacement parameters d_1 and d_2 are adjusted to realize each phase. **(b, e, h, k)** Simulated bulk band structures with eigenmodes color-coded by the Stokes parameter S_3, revealing polarization characteristics of each branch. Nonmagnet and antiferromagnet configurations show no polarization splitting, ferromagnet configuration shows momentum-independent splitting, while altermagnet configuration exhibit clear momentum-dependent splitting. **(c, f, i, l)** Corresponding simulated eigenfield intensity |E| (left) and phase arg(E) (right) distributions at selected wavevectors marked in the band structures.

Supplementary Note 7. Sample fabrication, simulations, and measurements.

To realize and validate the altermagnetic behavior experimentally, we fabricate a multilayer magnetophotonic crystal system designed to implement a stable and reconfigurable staggered magnetic bias (Supplementary Figures 9-10). The device consists of five functional layers: the top and bottom layers host patterned arrays of NdFeB permanent magnets; a perforated aluminium alignment plate beneath each magnet array ensures precise positioning and prevents lateral displacement caused by magnetic attraction or repulsion. The central layer contains the photonic crystal, composed of YIG cylindrical elements arranged on a square lattice with lattice constant a=40.0 mm. Each YIG element has a diameter of 6.0 mm and a height of 2.5 mm. To implement the required structural offset, the unit cell incorporates eight semicircular elements, satisfying a displacement difference of $d=d_1-d_2=0.1a$.

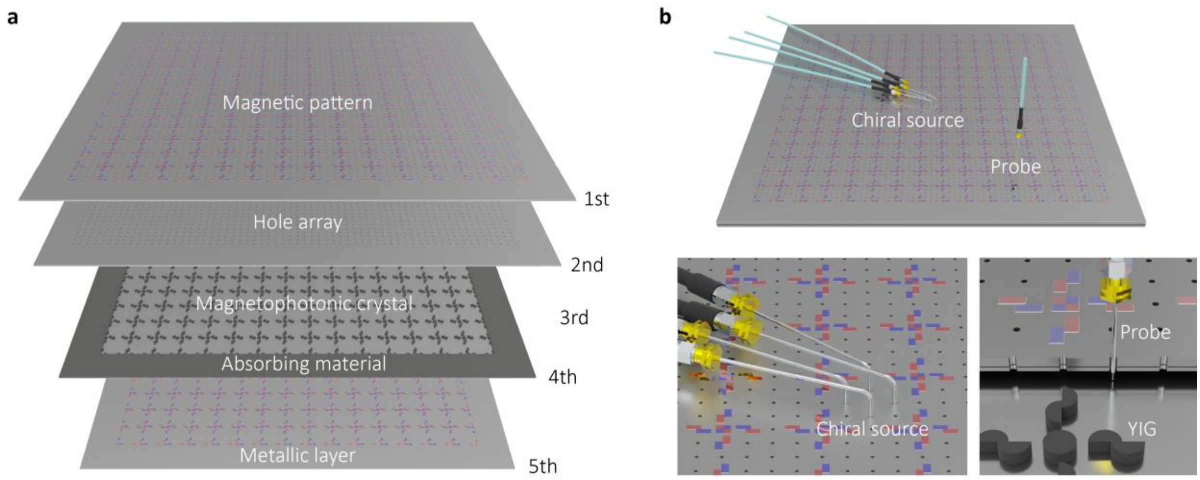

Supplementary Figure 9 | Schematic of the experimental sample and the excitation-detection configuration. (a) The device consists of five layers: (1) the top magnetic pattern formed by the rectangular array of permanent magnets, (2) a perforated hole array layer for precise alignment and mechanical anchoring of the magnets, (3) the central magnetophotonic crystal layer containing the YIG rods, (4) an absorbing material layer for suppressing boundary reflections, and (5) the bottom metallic layer providing electromagnetic confinement and structural stability. This multilayer design enables accurate, stable, and reconfigurable implementation of spatially alternating magnetic bias across the photonic crystal lattice. **(b)** Chiral excitation and detection. A four-probe chiral source array is used to generate the desired handed excitation. A single dipole probe is then inserted into selected holes to map the local electric field distribution.

Permanent magnets of two sizes (6 mm × 3 mm and 3 mm × 3 mm, height 2.0 mm) provide localized magnetic bias, and a staggered orientation along ±z is programmed by manually flipping individual magnets. An absorbing layer is inserted beneath the photonic crystal to suppress unwanted reflections, and the bottom metallic plate forms a parallel-plate waveguide that supports only TM modes with out-of-plane electric field $E_z \neq 0$. Access holes (diameter 1.5 mm) in the upper alignment plates allow insertion of coaxial probes for field excitation and measurement. Photographs with and without a magnetic viewing film (Supplementary Figure 10) confirm the alternating magnetization pattern and the accurate alignment of gyromagnetic elements.

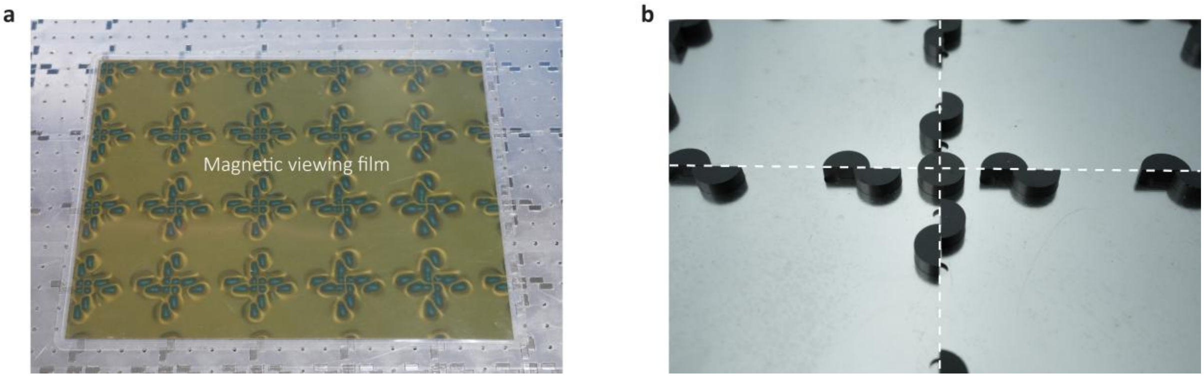

Supplementary Figure 10 | Photographs of the fabricated sample. (a) Configuration covered with a magnetic viewing film, visualizing the alternating magnetic field intensity pattern imprinted by the patterned permanent magnets. **(b)** Close-up of the YIG elements at the four corners of a unit cell, illustrating the precise alignment of gyromagnetic elements for generating spatially alternating magnetic bias.

Supplementary Note 8. Measured magnetic hysteresis loop of the gyromagnetic material.

The gyromagnetic cones are fabricated using commercially available yttrium iron garnet (YIG) supplied by WESTMAG TECHNOLOGY COPROPATION Limited (Mianyang, China). The magnetic properties of the gyromagnetic materials are investigated at room temperature, and the measured M-H hysteresis loop is provided in Supplementary Figure 11. The data reveal that the gyromagnetic elements become magnetized and reach saturation once the applied magnetic field exceeds approximately 700 Oe. For completeness, the M-H loop is measured and recorded up to 3000 Oe.

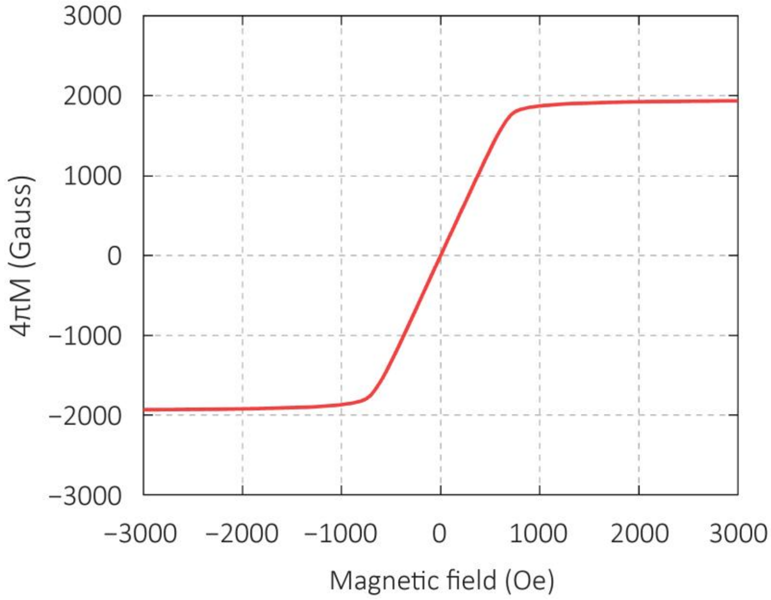

Supplementary Figure 11 | Magnetization curve of YIG material. Measured magnetic hysteresis loop of the YIG used in the magnetophotonic crystal. The vertical axis shows the saturation magnetization $4\pi M$ as a function of the applied magnetic field. The YIG exhibits a saturation field of approximately 700 Oe, ensuring sufficient magneto-optical response under the external magnetic bias employed in the experiment.

Supplementary Note 9. Bulk bands under zero and nonzero net magnetization.

(1) Zero net magnetization.

To assess the robustness of the altermagnetic polarization splitting under realistic perturbations, we systematically analyze two key parameters in the magnetically compensated configuration: the structural displacement and the magnetic-bias strength. Supplementary Figure 12 examines the effect of varying the geometric displacement at a fixed magnetic bias. Increasing or decreasing d away from the nominal value d=0.1a only weakly modifies the band curvature but preserves the polarization splitting near the M point, demonstrating that the altermagnetic response is insensitive to moderate geometric variations.

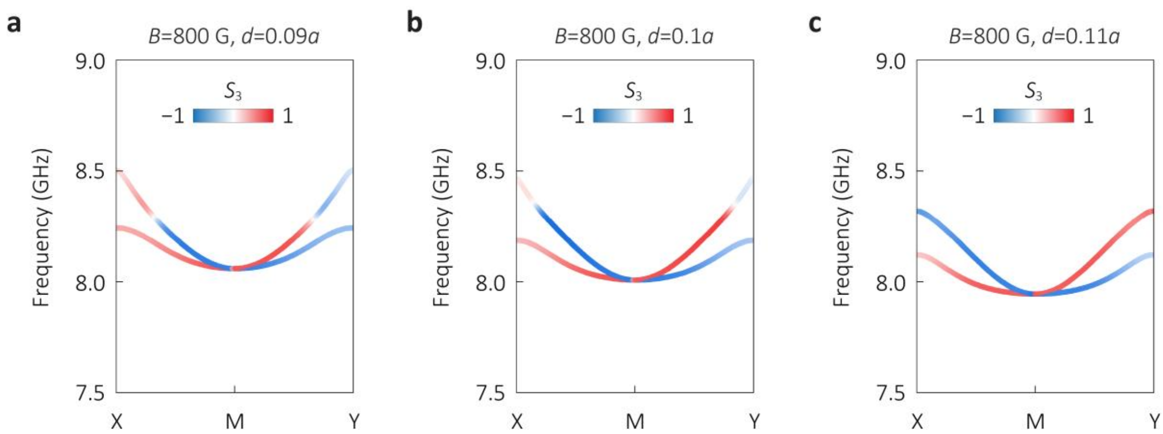

Supplementary Figure 12 | Influence of displacement d on polarization splitting in the altermagnetic photonic crystal. Simulated bulk band structures of the altermagnetic configuration under a fixed magnetic bias B=800 G for different displacement values: **(a)** d=0.09a, **(b)** d=0.1a, and **(c)** d=0.11a.

Supplementary Figure 13 evaluates the influence of magnetic-bias strength for a fixed displacement d=0.1a. Across the tested range B=750~850 G, the momentum-dependent LCP-RCP splitting remains clearly visible with only slight shifts in frequency. Together, these results confirm that the photonic altermagnetic phase is simultaneously robust against both structural offsets and magnetic-bias fluctuations under compensated magnetization.

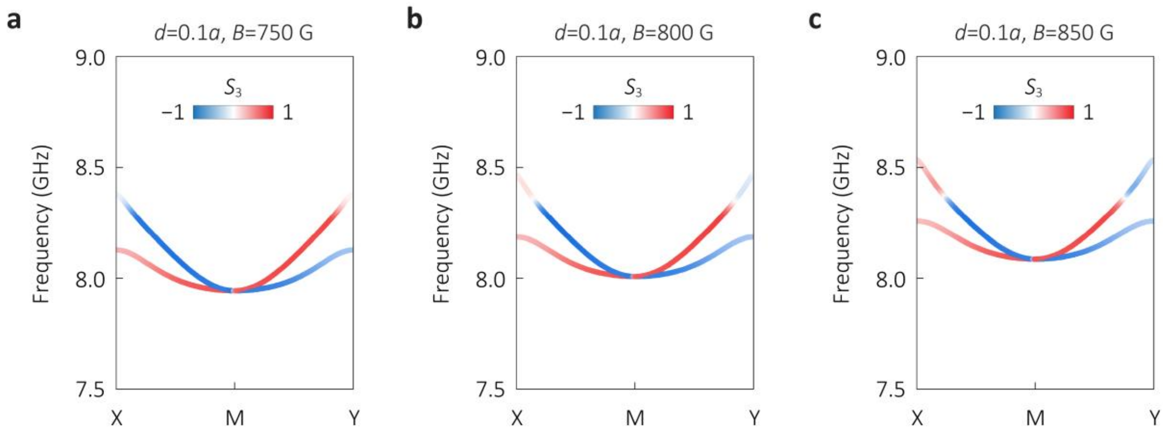

Supplementary Figure 13 | Influence of magnetic bias on polarization splitting in the altermagnetic photonic crystal. Simulated bulk band structures for a fixed displacement d=0.1a under varying magnetic bias strengths: **(a)** B=750 G, **(b)** B=800 G, and **(c)** B=850 G.

(2) Nonzero net magnetization.

To further examine how departures from perfect compensation affect the altermagnetic response, we investigate two distinct forms of symmetry breaking: rotational-symmetry imbalance in the structural displacement and magnetic-bias imbalance between the two sublattices. Supplementary Figure 14 shows that when the displacements along the two orthogonal directions become unequal ($d_a \neq d_b$), the fourfold rotational symmetry protecting the M-point degeneracy is partially lifted. As the asymmetry increases, the previously symmetric spin-split branches become distorted and the degeneracy at the M point gradually shifts and weakens, indicating that polarization splitting remains present but no longer follows the ideal altermagnetic form.

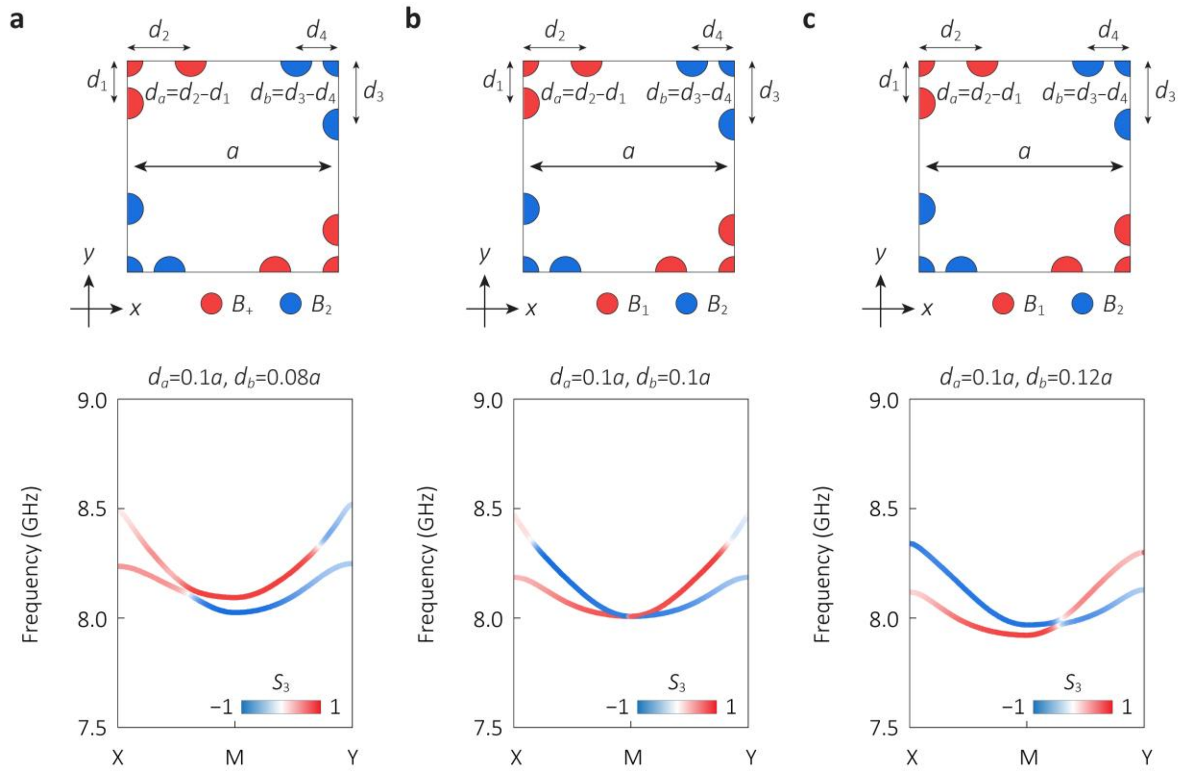

Supplementary Figure 14 | Rotational symmetry breaking on altermagnetic polarization splitting. (a-c) Structural configurations and corresponding photonic band structures under staggered magnetic bias with unequal displacements d_a and d_b. **(a)** d_a=0.1a and d_b=0.08a. **(b)** d_a=0.1a and d_b=0.1a. **(c)** d_a=0.1a and d_b=0.12a.

Supplementary Figure 15 examines the second mechanism: magnetic non-compensation. When the two sublattices carry perfectly opposite magnetic biases (B_1=−B_2=800 G), the system preserves the compensated altermagnetic configuration and exhibits a clean degeneracy at the M point with symmetric momentum-dependent polarization splitting. Introducing a slight imbalance (B_1=800 G and B_2=−750 G) breaks this compensation condition and immediately lifts the degeneracy, causing noticeable band bending and unequal separation between the two polarization branches. This behavior underscores that the altermagnetic splitting in photonic systems relies on both staggered magnetization and global magnetic compensation: once this balance is perturbed, the characteristic symmetry-protected band features deform, and the M-point degeneracy is no longer preserved.

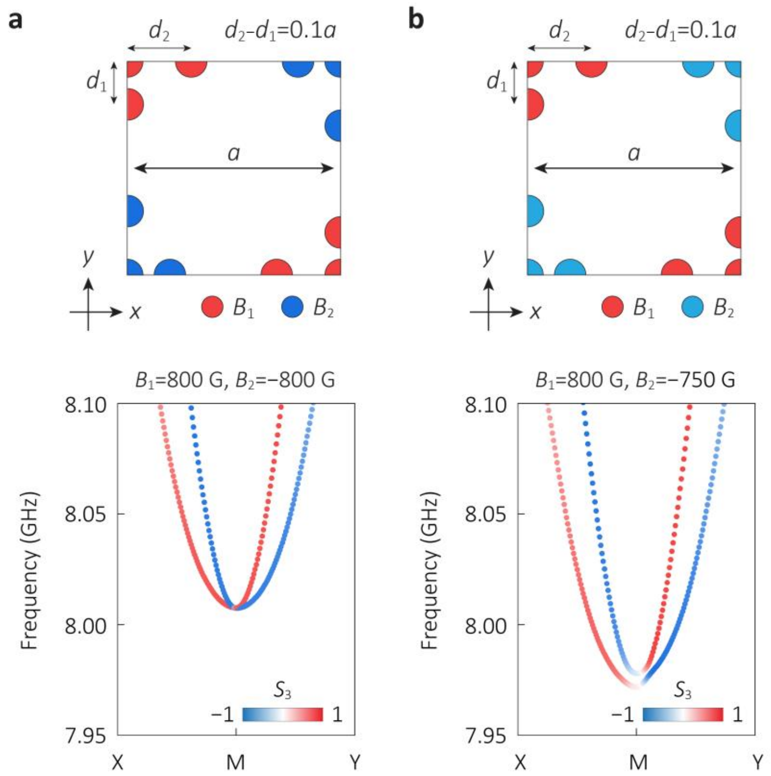

Supplementary Figure 15 | Influence of magnetic compensation on polarization splitting. **(a)** Perfect magnetic compensation with B_1=800 G and B_2=−800 G. **(b)** Slight imbalance between the two sublattices with B_1=800 G and B_2=−750 G.

Supplementary Note 10. Numerical simulations of chiral sources.

Supplementary Figure 16 illustrates the generation, and spatial characteristics of the circularly polarized excitation used in our numerical simulations. Four-point emitters arranged at the corners of a square are driven with successive phase delays of $\pi/2$, producing left-circularly polarized (Supplementary Figure 16a) and right-circularly polarized (Supplementary Figure 16b) sources. The left panels show the imposed phase pattern for each configuration, while the right panels display the simulated out-of-plane electric-field distribution E_z at 8.10 GHz. The resulting spiral wavefronts confirm that the four-element phase array generates clean and well-defined circular polarization, providing controlled excitation for probing the spin-dependent photonic bands.

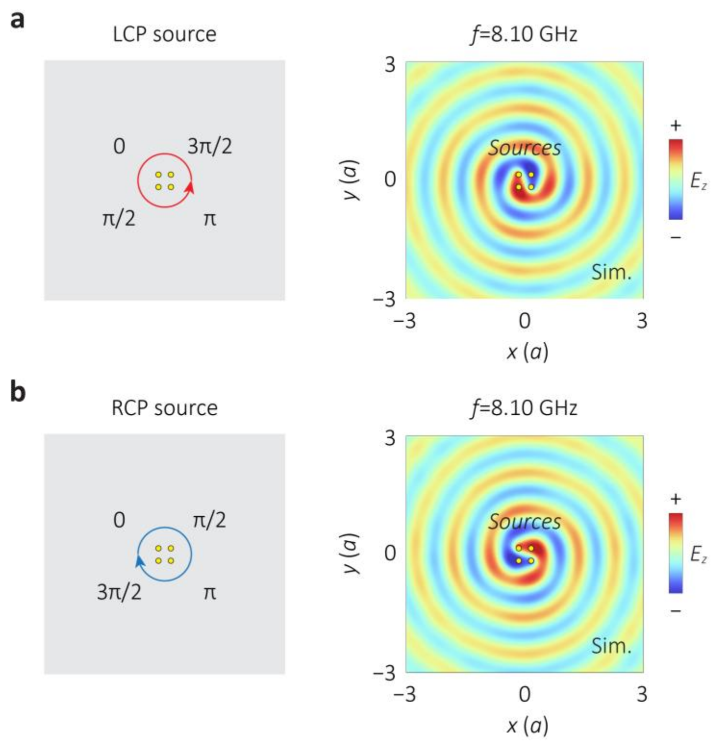

Supplementary Figure 16 | Simulated near-field distributions for circularly polarized sources. (a) Left-circularly polarized source and **(b)** right-circularly polarized (RCP) source generated using four phase-controlled point emitters with phase delays of $\pi/2$ between adjacent elements.

Supplementary Note 11. Finite-size effects on bulk bands.

Supplementary Figure 17 evaluates how the finite lateral extent of the photonic crystal affects the extracted polarization-resolved dispersion. As the lattice size increases, the spectral features become progressively smoother and the momentum resolution improves, yet the essential band characteristics, such as the preservation of the M-point degeneracy and the alternating polarization pattern, remain invariant. This demonstrates that the observed altermagnetic signatures originate from bulk symmetry properties rather than boundary-induced or size-dependent effects.

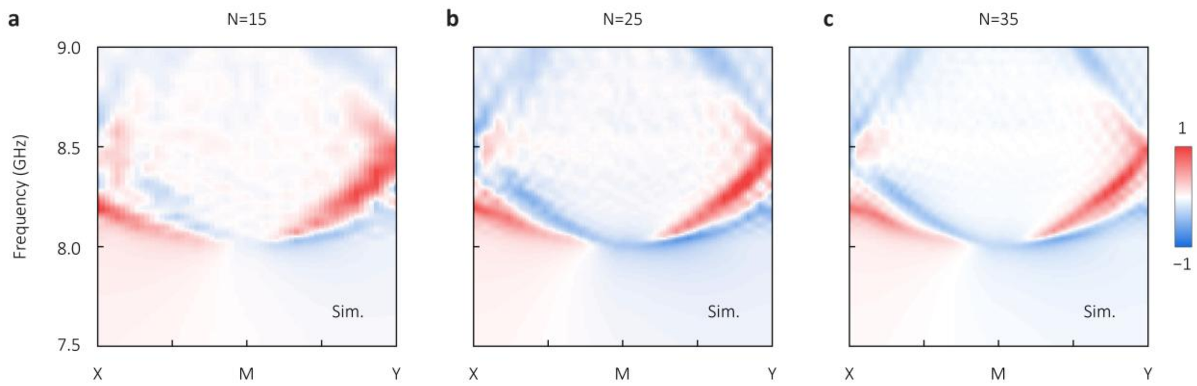

Supplementary Figure 17 | Finite-size effect on the polarization-resolved band structure. Simulated dispersion of the photonic altermagnet with different lattice sizes: (a) N=15, (b) N=25, and (c) N=35 unit cells along each direction.

Supplementary Note 12. Bulk band under magnetic reversal and compensation conditions.

Reversing the external magnetic field provides a direct test of whether the observed polarization splitting originates from genuine time-reversal-symmetry breaking rather than geometric chirality, and this reversal flips the two polarization branches in exact analogy to how electronic spin states invert under magnetic-field reversal. Flipping the magnetization of all gyromagnetic elements (interchanging the B_1 and B_2 sublattices) inverts the local circular-polarization preference of each element (Supplementary Figure 18). The momentum-dependent polarization splitting, the M-point degeneracy enforced by the compensated magnetic pattern, and the overall band curvature all remain unchanged.

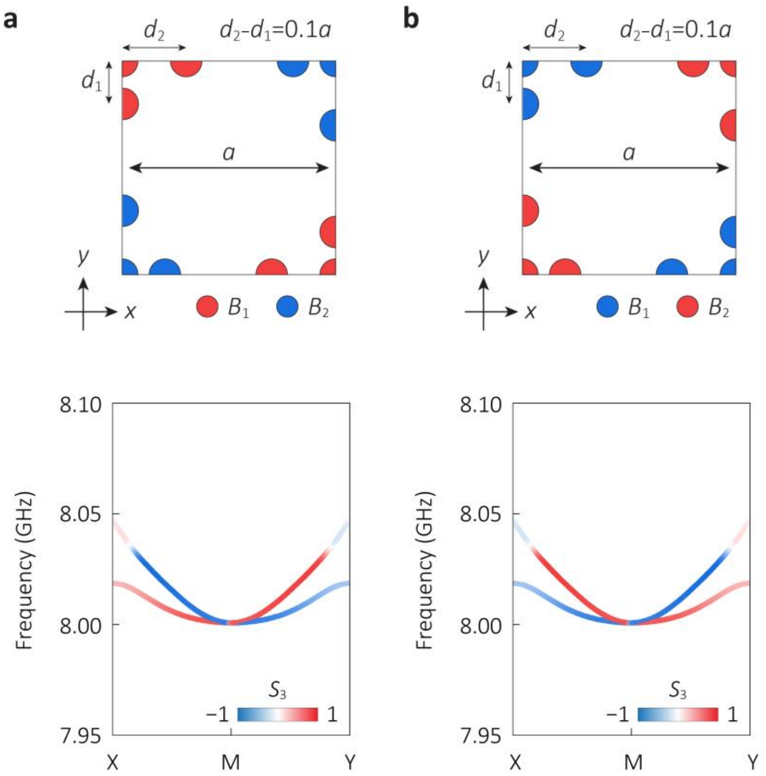

Supplementary Figure 18 | Effect of reversing the external magnetic field on the altermagnetic band. Two magnetization configurations obtained by flipping the external bias applied to all gyromagnetic elements.

Supplementary Note 13. Finite-size effects on isofrequency contours.

Supplementary Figure 19 examines how the finite lateral size of the photonic crystal influences the momentum-space extraction of polarization splitting. As more unit cells are included, the reconstructed Fourier spectra become progressively cleaner: spurious side lobes diminish, the contours sharpen, and the contrast between opposite polarizations becomes more pronounced.

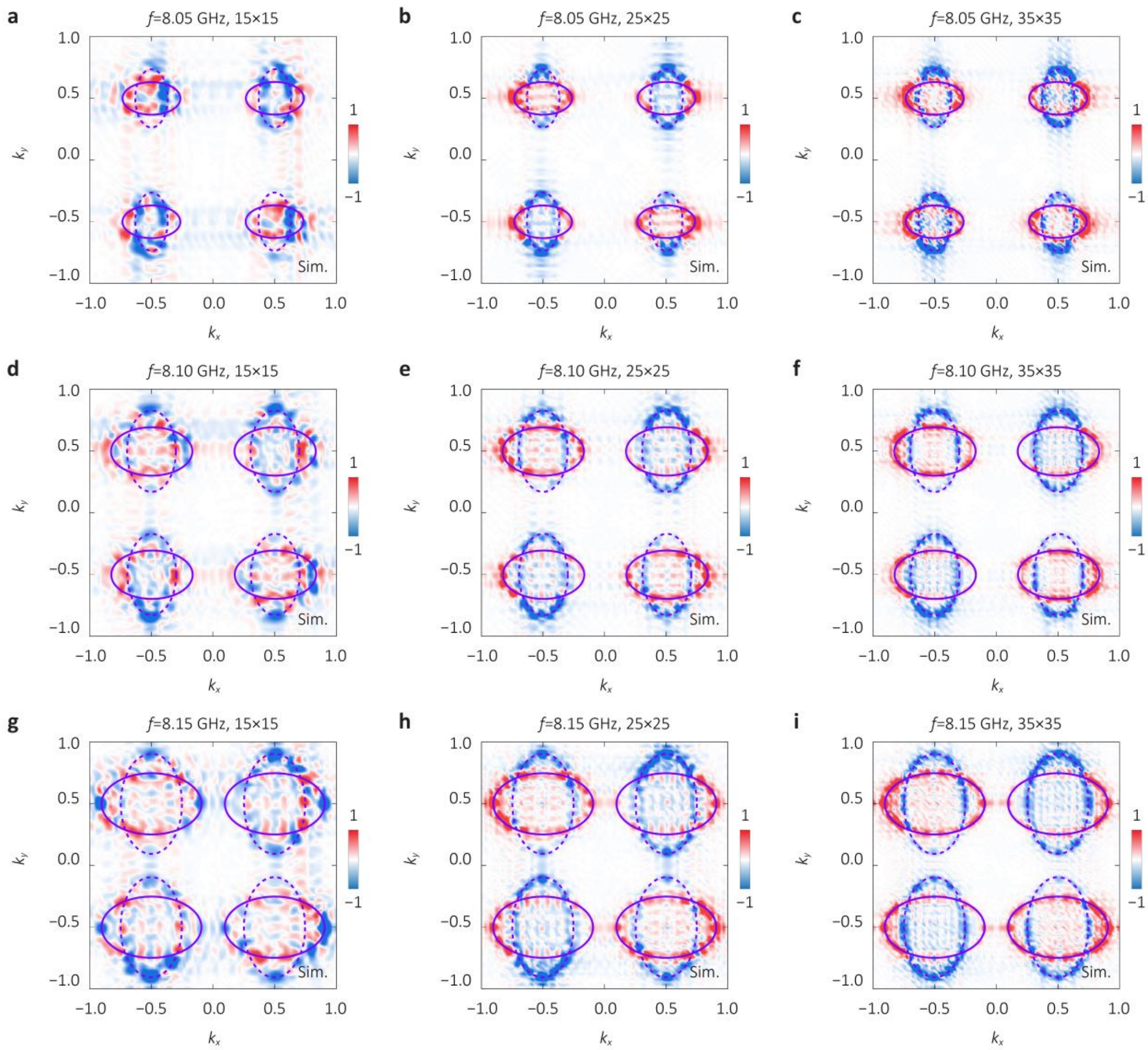

Supplementary Figure 19 | Influence of sample size on the observed momentum-resolved polarization splitting. Simulated Fourier-space S_3-resolved field distributions for photonic crystals of different sizes: **(a, d, g)** 15×15 unit cells, **(b, e, h)** 25×25 unit cells, and **(c, f, i)** 35×35 unit cells. Results are shown at frequencies **(a-c)** 8.05 GHz, **(d-f)** 8.10 GHz, and **(g-i)** 8.15 GHz. The overlaid solid and dashed purple contours represent the corresponding simulated isofrequency lines. Larger sample sizes yield sharper momentum features and improved contrast in polarization separation, confirming that the observed altermagnetic-like splitting is robust and not a finite-size artifact.

Importantly, the characteristic separation of LCP and RCP responses persists for all sample sizes studied, indicating that the observed altermagnetic-like splitting originates from bulk symmetry properties rather than from edge effects or insufficient sampling in real space. The systematic improvement with increasing system size confirms that the experimental procedure captures genuine bulk polarization behavior.

Supplementary Note 14. Repeated measurements and error analysis.

Supplementary Figure 20 characterizes how the choice of intermediate-frequency (IF) bandwidth affects the quality of the measured transmission signals. Reducing the IF bandwidth substantially suppresses both amplitude and phase fluctuations, resulting in a significantly lower noise floor and noticeably cleaner spectral traces. This improvement is crucial because the Fourier-space reconstruction of polarization-resolved bands relies sensitively on phase stability. The comparison shows that using a narrower 3 kHz bandwidth yields data of much higher fidelity than the 100 kHz setting, enabling a more reliable extraction of the altermagnetic polarization splitting.

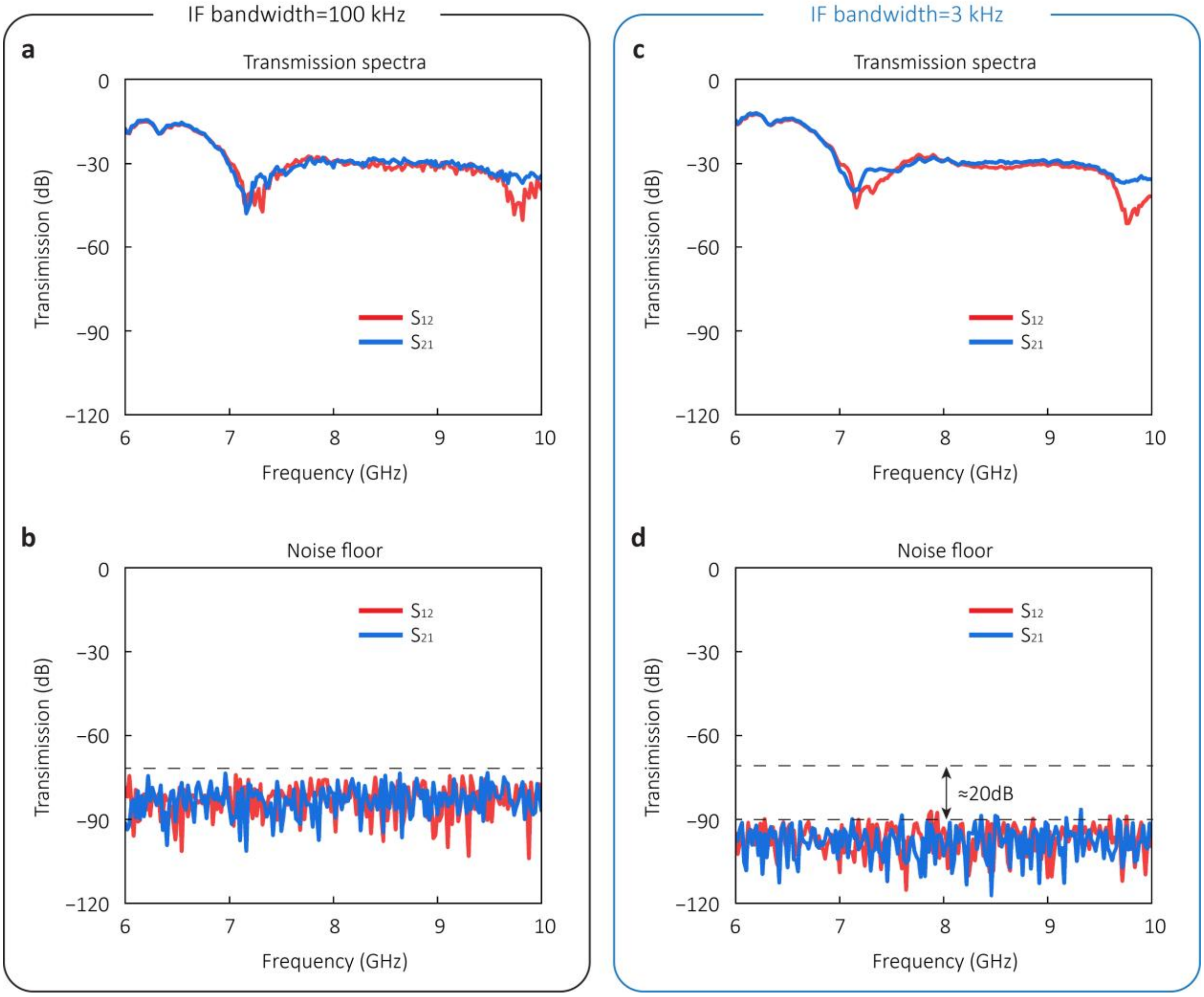

Supplementary Figure 20 | IF bandwidth on signal transmission and noise characteristics. Measured transmission spectra (S_{12}, S_{21}) and corresponding noise floors under different intermediate-frequency (IF) bandwidth configurations. (a-b) Results obtained with IF bandwidth=100 kHz. (c-d) Results obtained with IF bandwidth=3 kHz. The use of a narrower IF bandwidth effectively reduces both amplitude and phase noise, lowering the noise floor by approximately 20 dB.

Supplementary Figure 21 verifies the reproducibility of the polarization-resolved measurements and illustrates how reducing the IF bandwidth improves data quality. After fully disassembling and reassembling the sample twice, the momentum-resolved LCP/RCP spectra remain consistent, demonstrating that the observed polarization splitting is robust against assembly variations. Moreover, using a narrower 3 kHz IF bandwidth significantly enhances the signal clarity and suppresses background fluctuations compared with the 100 kHz setting, allowing the polarization contrast to be resolved with much higher fidelity.

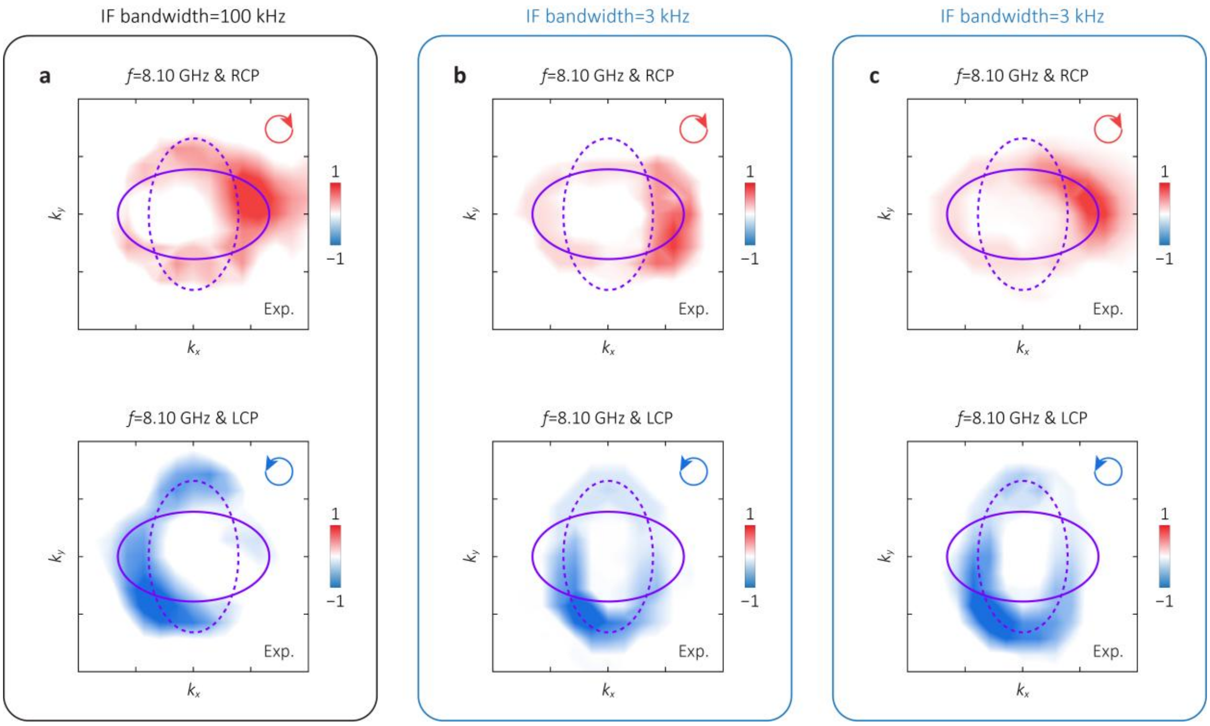

Supplementary Figure 21 | Reproducibility and effect of IF bandwidth on polarization measurements. Experimentally measured momentum-resolved polarization distributions for LCP and RCP at f=8.10 GHz under different IF bandwidth configurations. **(a)** Measurement with IF bandwidth=100 kHz; **(b-c)** Measurements with IF bandwidth=3 kHz after two independent disassembly and reassembly cycles.

We introduce positional disorder into the simulations to quantitatively evaluate its influence. Since the polarization splitting primarily originates from the geometric offset parameter d, we defined the perturbed displacement as $d'=d_0+\delta\cdot\xi\cdot a$, where d_0 is the nominal offset of the semicylinders, δ represents the fluctuation strength (ranging from 0 to 0.04), ξ is a random number uniformly distributed between −1 and 1, and a is the lattice constant. Supplementary Figure 22 examines how positional disorder affects the robustness of the altermagnetic polarization splitting. As the displacement noise increases from δ=0 to δ=0.04, the top-row magnetic patterns show local snapshots of the perturbed bias configuration, although only a small region is visualized, the global arrangement is fully randomized across the lattice.

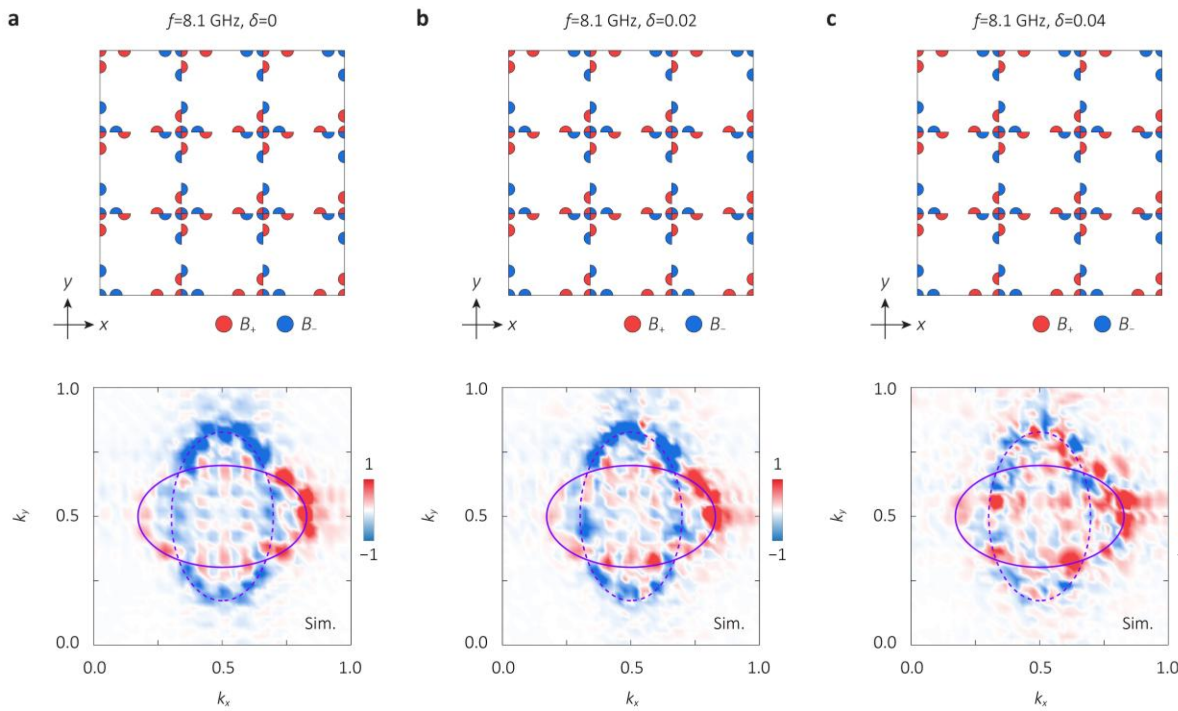

Supplementary Figure 22 |. Structural disorder on polarization splitting. Real-space magnetic configurations (top) and corresponding polarization distributions (bottom) at f=8.10 GHz for different levels of positional disorder: **(a)** δ=0, **(b)** δ=0.02, and **(c)** δ=0.04. Red and blue circles denote opposite magnetic bias directions.

The actual fabrication tolerance of our sample is ±0.05 mm. In the simulations, even with perturbations up to 0.02a (0.40 mm), eight times larger than the experimental uncertainty, clear polarization splitting remains observable. Only when the perturbation increases to about sixteen times the actual position error does the polarization mixing start to appear. The robustness stems from the global nature of the polarization splitting: the excitation wavelength ($\approx$3.7 cm at 8.1 GHz) is vastly larger than the fabrication-induced positional deviations (±0.05 mm), making the effect insensitive to local imperfections. These results confirm that the observed polarization splitting originates from a global altermagnetic mechanism that remains stable against realistic fabrication tolerances.

Supplementary Figure 23 evaluates how uniform background loss influences the momentum-resolved polarization splitting. As the artificial loss parameter increases from 0 to 0.025, the Fourier-domain intensity gradually decreases and the features become more diffuse, reflecting the expected linewidth broadening from added dissipation. Importantly, the characteristic left–right circular polarization contrast remains clearly visible across all tested loss levels, demonstrating that the altermagnetic-like splitting is an intrinsic property of the gyrotropic pattern rather than a consequence of loss-related artifacts.

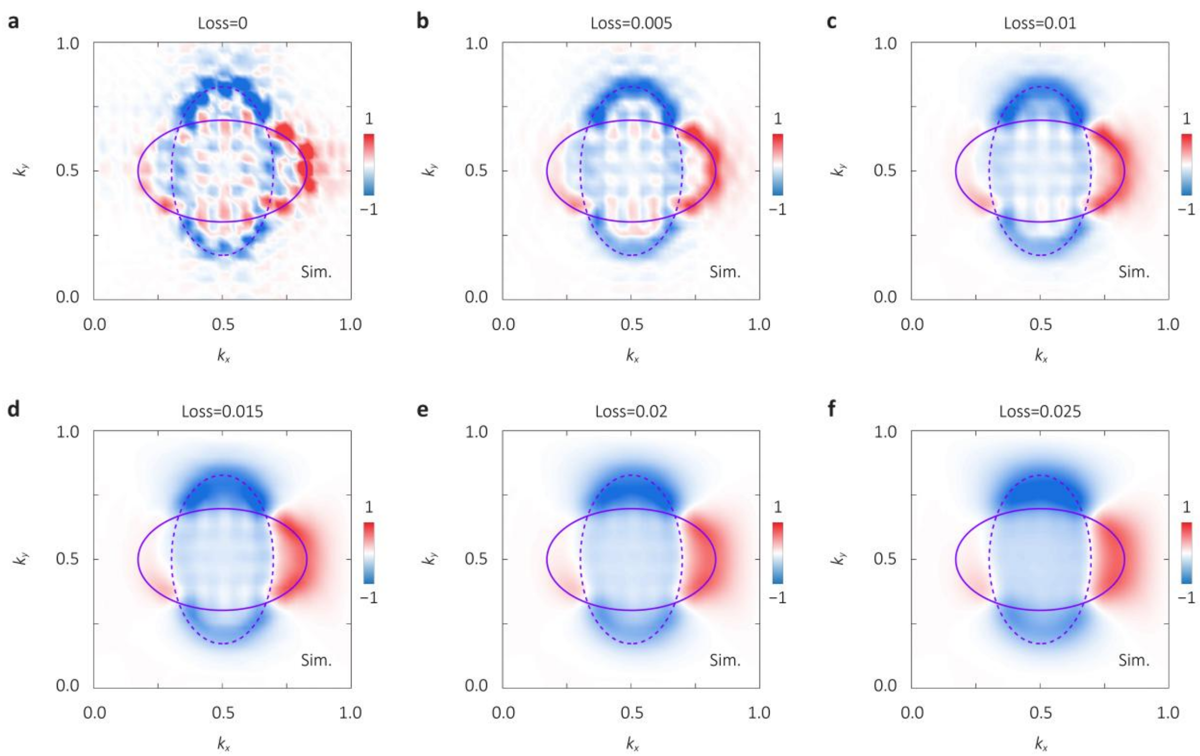

Supplementary Figure 23 | Background loss on polarization splitting. Simulated momentum-resolved distributions under different background loss levels: (a) 0, (b) 0.005, (c) 0.01, (d) 0.015, (e) 0.02, and (f) 0.025.